Effects of composition and microstructure on oxidation and stress corrosion cracking susceptibility of stainless steel claddings in hydrogenated PWR primary water

Tongming Cui[1, 2], Xinhe Xu[1, 2], Jiarong Ma[1,2], Zhanpeng Lu[1, 2, *], Yuanjie Tang[1,2], Kun Zhang[1, 2], Shuangliang Yang[3], Zhiming Zhong[3], Sergio Lozano-Perez[4], Tetsuo Shoji[5]

1. Institute of Materials, School of Materials Science and Engineering, Shanghai University, Shanghai, 200072, China
2. State Key Laboratory of Advanced Special Steels, Shanghai University, Shanghai, 200072, China
3. State Nuclear Power Plant Service Company, 888 Tianlin Road, Shanghai 200233, China
4. Department of Materials, University of Oxford, Parks Road, OX1 3PH, Oxford, UK
5. New Industry Creation Hatchery Center, Tohoku University, Sendai 980-8579, Japan

*Corresponding author: Zhanpeng Lu, zplu@t.shu.edu.cn

Abstract

Oxidation resistance and stress corrosion cracking (SCC) susceptibility of A508III-309L/308L stainless steel (SS) claddings were investigated in simulated pressurized water reactor (PWR) primary water following a microstructure characterization. Preferential oxidation of slip bands was observed in 309L SS. The oxidation resistance of 309L SS was found to be lower than that of 308L SS due to the higher Cr- and ferrite-content in 308L SS than in 309L SS after cladding. There was no indication of SCC for low alloy steel (LAS) after slow strain rate tensile (SSRT) tests. The presence of type-I and type-II boundaries, composition dilution and less δ-ferrite content synergistically contributed to increasing the SCC susceptibility of 309L SS cladding. The effect of chemical composition and microstructure on SCC performance of the SS claddings was discussed.

Keywords: Pressurized water reactor, stainless steel cladding, oxidation, stress corrosion cracking, ferrite

1. Introduction

Due to superior mechanical property, weldability, fabricability, and corrosion resistance, Austenitic stainless steel (ASS) welds containing austenite and ferrite phases, are widely applied as critical components in many industries [1–6]. Also, the weld deposition of stainless

steel on low alloy steels (LAS), called SS weld overlay cladding such as 308L SS and 309L SS, is frequently selected to clad on the inside of the reactor pressure vessel (RPV) as a protective barrier against the reaction with the high-temperature water. Apart from preventing corrosion, the weld overlay cladding also has structural integrity functions [7]. Stress corrosion cracking (SCC) is the potential degradation mode for the claddings and dissimilar metal welded joints [8−11]. The effects of post-weld heat treatment [12,13], water chemistry [9,13,14], thermal aging [5,15−17], microstructure evolution [10,18−20] and dilution ratio [21] on mechanical properties and SCC performance of weld metals have been reported extensively. However, the effect of microstructure evolution and chemical composition on oxidation resistance, mechanical property and SCC performance of the stainless steel claddings have attracted little attention. The properties of oxide films are considered to be critical for SCC initiation and crack propagation of the critical components during operation in high-temperature water. Experimental results in previous works show that crack propagation in many systems was related to the oxidation that occurs when the protective oxide film in the vicinity of the crack tip was ruptured [22,23]. The morphology, chemical compositions and microstructure of the oxide films grown on the SS claddings surface in contact with high-temperature water have been reported [24−26].

There are many ways of determining the SCC performance of metal or alloy in high-temperature water, such as crack growth rate (CGR) tests with compact tension specimens, constant load with tensile specimens, constant strain tests with U-bend, C-ring, or other specimens, and slow strain rate tensile (SSRT) tests. The initial SSRT strain rates used depend on several factors, such as the alloy-environment system, the experimental variables, and the test objectives [27]. In the current study, the microstructure evolution of the LAS-SS cladding layers near the fusion boundary (FB) has been characterized and the properties of the oxide film developed on SS cladding layers are analyzed by scanning electron microscope (SEM) and transmission electron microscopy (TEM). The SCC susceptibility of the A508III-308L/309L SS claddings in hydrogenated PWR primary water has been investigated by SSRT tests.

2. Experimental

2.1. Materials and microstructure characterization

The materials used in this work were LAS-SS cladding layers taken from the RPV inner wall. The main chemical compositions of the A508III, 309L SS, and 308L SS measured by direct reading spectrometer are listed in Table 1. The location for measuring the chemical composition of the 309L SS cladding was about 1.8 mm away from the fusion boundary. The red box 1 indicated the sampling location for microstructure analysis, including optical microscope observation, microhardness test, SEM and energy dispersive spectroscopy (EDS) analysis, the specimens with a dimension of 20 mm × 8 mm × 2.2 mm; The red box 2 indicated the sampling location of 309L/308L SS welds for exposure tests with a size of 10 mm × 10 mm × 2.2 mm, as shown in Fig.1. Microhardness was measured with HXD-1000TMC/LCD microhardness tester using a 200 gf force and a holding time of 15s. Three microhardness lines were acquired with approximately 130 points per line. Prior to the microstructure analysis, the specimens were ground to a 2000-grit surface finish with SiC waterproof papers, then mechanically polished with a 1-μm diamond suspension. For metallographic observation, the LAS side was chemical-etched use 4% nital solution of about 8 s, and the SS side was electro-etched in 30% sodium hydroxide solution for 40 s by applying a direct-current voltage of about 5V. The distribution of C, Cr, Fe and Ni close to the FB was measured by electron probe microanalysis (EPMA)-8050G (Shimadzu instrument), operating at 15 kV. The scanning region was 320 μm × 596 μm with a sampling time of 1.0 ms/point. The electron backscatter diffraction (EBSD) images were obtained via an Apollo 300 field-emission SEM operated at 20 kV. The step size was set to 0.2 μm for A508III and 5 μm for 309L SS.

2.2. Exposure and SSRT tests in high-temperature water

The schematics of the exposure and SSRT tests autoclave setup used is shown in Fig. 2. The solution for the exposure tests was prepared by adding 2.2 mg/L Li in $LiOH{\cdot}H_2O$ and 1200 mg/L B in H_3BO_3 to ultra-pure water (resistivity ≥18.2 MΩ·cm). The dissolved oxygen concentration in the solution was kept to be below 5 μg/L by purging high-purity nitrogen gas (≥99.999%) before heating up the autoclave. The concentration of dissolved hydrogen (DH) was maintained at 2.6 ppm by controlling a hydrogen gas overpressure of about 0.07 MPa in the water storage tank during the whole test procedure. The internal pressure of the autoclave was kept at 13.5 ± 0.1 MPa applied via a high-pressure pump. A pre-oxidation for 48 h was performed after the internal temperature of the autoclave reached the target temperature (325 °C)

under hold mode, then the loading system for SSRT tests was started. The SSRT specimens were taken from various locations of the LAS-SS weld metals. The A508III base metal SSRT specimen was cut far away from the FB named A508-MS. The transition layer SSRT specimen was cut near the FB named A508-TS. The 309L/308L SSRT specimen contained a 309L layer and 308L inner layer, as shown in Fig. 3(a). All the tensile specimens had a gauge size of 15 mm × 4 mm × 2.2 mm, as shown in Fig. 3(b). The strain rate for SSRT tests was set at 3×10^{-7}/s and 1.0×10^{-6}/s, respectively. The engineering stress-strain curves were drawn of each specimen after SSRT tests. The exposure test was carried out under this condition for 500 h. Before exposure and SSRT tests, the surface of the specimens was ground using SiC papers finish to 1500 #, then rinsed with distilled water and ethanol.

2.3. Characterization of oxide films and fracture surfaces

The oxide films were characterized by extracting cross-sectional TEM specimen prepared via an FEI Helios 600i Nanolab focused ion beam (FIB)/SEM system, as shown in Fig. 4 [28]. A micron-level thickness of Pt was deposited on the selected region to protect the oxide film before Ga-ion beam sputtering. The thickness of the TEM lamellar specimen was milled from 2 μm to below 100 nm by Ga-ion beam sputtering, and then Pt-welded to copper support with five specimen sites. The cross-sectional oxide film specimens were characterized via a JEM-2100F TEM, operating at 200 kV. The chemical composition profile of the oxide film was analyzed by energy-dispersive X-ray spectroscopy (EDS) with an Oxford Instruments X-max 80TLE detector under the scanning TEM (STEM) mode. High-resolution TEM photograph and high angle dark-field (HAADF) photograph were also obtained. The fracture surfaces were observed using an Apollo 300 thermal field-emission SEM operated at 20 kV.

3. Results

3.1 Microstructure of the LAS-SS claddings

The elemental distributions with increasing distance from the FB were measured by EDS with an Apollo 300 thermal field-emission SEM, as shown in Fig. 5. A sharp drop of Fe and increases of Cr and Ni were observed in the 309L region close to the FB. The Cr and Ni concentrations in 308L SS were higher than those in 309L SS after welded. The microhardness measurement results of the LAS-SS claddings are shown in Fig. 6. There was a higher microhardness region in 309L SS near the weld FB. The microhardness in 309L was higher

than that in 308L SS. On the LAS side, the region about 4 mm from the FB had a relatively higher hardness value than the adjacent regions. The compositional profiles close to the fusion line measured by EPMA are shown in Fig. 7. A carburization region close to the FB was slightly enriched in iron and depleted in nickel and chromium.

The optical microstructure of the LAS, including the heat-affected zone (HAZ) and base metal, is displayed in Fig. 8. The HAZ had a complex structure with a width of approximately 4 mm. The region close to the fusion line at the A508III side revealed the coarse-grained characteristic consisting of ferrite and carbides, as shown in Fig. 8(a). The coarse-grained region was always formed accompanied by carbon depletion (decarburization) with a width of approximately 100 μm; the C-depleted region formed ascribed to the carbon mitigation to the fusion zone, as shown in Fig. 7 carbon-mapping. The LAS bulk metal showed the bainite microstructure containing dispersed lath ferrite, as shown in Fig. 8(d). A fine-grained zone was observed between the base metal and the coarse-grained zone, as shown in Figs. 8(b) and (c).

Figure 9 shows the metallographic structure of the fusion region and SS claddings. Type-I and type-II boundaries were found to be close to the FB. The type-II boundary was parallel to the FB with a distance of < 100 μm, usually appeared adjacent to the FB, and the Type-I boundary formed between the FB and type-II boundary perpendicular to the FB, as shown in Fig. 9(a). A semi-continuous martensite layer (dark region) was observed along the fusion boundary with a width of about 10-20 μm is shown in Fig. 9(a). Ferrites can be clearly seen in 308L SS. Using the metallographic method, the statistical results show that the δ-ferrite content was about 10.5% (vol. %) in 308L SS, which was much higher than that in 309L SS, as shown in Figs. 9(e), (f) and (g). The less ferrite content in 309L might be due to the effects of weld dilution (especially Cr element). Figure 10 shows the EBSD results of A508III and 309L SS near the FB. For LAS, the grains exhibited the random orientation, and the boundaries were mainly random grain boundaries (RGB). The Σ3 CSL grain boundaries were mainly distributed near the FB, as shown in Fig. 10(a) and (b). For 309L SS, the grains mainly show <001> preferred orientations, and the grain boundary types map showed that the grain boundary was mainly RGB, as shown in Fig. 10(c) and (d).

The SEM morphologies and EDS result from the ferrite in SS claddings, as shown in Fig. 11. It is evident that less dispersed worm-like ferrite is distributed in 309L SS, and network-like

ferrite in 308L SS. The ferrite has a higher Cr content and a lower Ni content than those of austenite. The microstructural evolution of the A508III-309L interface is observed by TEM, as shown in Fig. 12. There are many precipitates in the LAS side near the FB that showed the black block-like or rod-like, as shown in Figs. 12(b) and (c). The precipitates are $M_{23}C_6$ carbides, determined by high-resolution TEM imaging and selected area electron diffraction (SAED), as shown in Fig. 12(e) and pattern III [29]. The lath martensite in the FB zone and high-density dislocations in the SS can be seen by the TEM-bright field (BF) image, as shown in Fig. 12(d). The SAED pattern I and pattern II show the lattice characteristic of LAS base metal (bcc structure) and SS matrix (fcc structure).

3.2. Properties of the oxide films formed on SS claddings

Figure 13 shows the SEM morphologies of the oxide films grown on 309L and 308L specimens after immersion in simulated PWR primary water at 325 °C for 500 h. Dispersed large oxide particles on the 309L specimen surface with an average size of approximately 1 μm, while small compact ones seemed to be sub-surface, as showed in Figs. 13(d) and (e). The large faceted oxide particles formed on 308L surface were inhomogeneous and fewer than similar ones on 309L, as showed in Figs. 13(b) and (c). Compared with 309L, the size of the oxide particles grown on 308L was relatively smaller. The surface state of 308L after exposure was clearly visible.

Figure 14 shows a STEM-HAADF image of the oxide film grown on 309L. The oxide film developed on 309L displayed a double-layer structure. Large and loose oxide particles were distributed on the external layer, while the internal oxide was relatively compact. Localized stress/strain concentration caused some deformation/slip bands in the 309L matrix. Figures 15 and 16 show the higher magnification STEM-HAADF images and EDS results of the oxide film formed on 309L specimens. The oxide film had two-layers with the external oxide layer rich in Fe and the internal oxide layer rich in Cr. Some voids were clearly observed within the internal oxide film, as shown in Figs. 15(a) and 16(a). The oxidized regions of the deformation/slip bands consisted of Cr-rich oxides, as shown in Fig. 15(a). Ni-enrichment was observed at the oxide/matrix boundary (depleted in Cr and Fe), as shown in Fig. 16. The average Cr concentration (~17% at.) of the internal oxide film was slightly lower than that of the matrix shown in Figs. 15(b) and 16(b). The thickness of the internal oxide film grown on

309L was 200 ± 40 nm based on the measurements on the area of about 2 μm width. The matrix underlying the oxide was austenite (fcc structure).

Figure 17 shows the STEM-HAADF images and EDS results of the oxide film formed on 308L specimen. It can be seen that Ni-enrichment (and Fe-Cr-depletion) had occurred at the oxide/matrix boundary. The external oxide film was enriched in Fe with some Cr. The average Cr concentration (~20% at.) of the internal oxide film was close to that of the matrix shown in Fig. 17(b). The thickness of the internal oxide film formed on 308L was 70 ± 30 nm based on the measurements on the area of about 2 μm width. The matrix beneath the oxide was austenite (fcc structure), as identified by TEM. The STEM-HAADF images of the grain boundary, EDS results of the oxide film and TEM-BF photograph of the grain boundary and oxide film grown on 308L are shown in Fig. 18. It was evident that the oxide layer thickness on austenite grains with different orientations was different. The influence of grain orientation on the oxidation of stainless steel in a simulated primary water environment has been widely reported (e.g., by Matthews et a. [30]) and will not be discussed any further in the present paper. The oxide film structure did not changed, exhibiting a double-layer structure with Fe-rich oxides in the external layer and Cr-rich in the internal layer. Ni was slightly enriched at the interface between oxide and matrix. The Cr content in the inner oxide layer was 20 ± 2% at., as observed in the EDS quantitative line scan showed in Fig. 18(b). The grain boundary was enriched in Cr and C, and depleted in Fe and Ni, as expected after chromium-carbide ($M_{23}C_6$) precipitation. Localized oxidation at the grain boundary was observed.

3.3. SCC susceptibility of LAS-SS claddings

Figure 19 shows the stress-strain curves after SSRT at 3×10^{-7}/s for A508III matrix and transition layer specimens in hydrogenated PWR primary water at 325 °C. It can be found that the elongation to failure for A508III transition layer specimen after SSRT at 3×10^{-7}/s in normal PWR primary water was 21.0%, while it was 26.9% for A508III bulk metal. The yield strength (YS) was determined by 0.2% off-set method from the stress-strain curve. The YS was 500 MPa for the A508III transition layer and 450 MPa for the base metal. The ultimate tensile strength (UTS) of LAS base metal (680 MPa) was lower than that of the transition layer (740 MPa). The higher YS, UTS and lower elongation to failure of A508III transition layer due to

the complex microstructure, carbide precipitates and carbon migration caused by welding heat-affected.

Figure 20 shows the SEM morphologies of the fracture surface after SSRT at 3×10^{-7}/s for A508-MS specimen in hydrogenated PWR primary water at 325 ºC. Specimen necking was observed. The fracture surface was uneven and covered by oxide. A shear-like ductile fracture with different size dimples, macro-voids and small amounts of secondary cracks was observed. Macro-voids and secondary cracks formation were always related to non-metallic inclusions such as MnS and Al_2O_3 [31]. There was no apparent SCC indication in the fracture region. Figure 21 shows the SEM morphologies of the fracture surface after SSRT at 3×10^{-7}/s for A508-TS specimen in hydrogenated PWR primary water at 325 ºC. The fracture surface was divided into two parts; the white index line indicated the fusion region and showed the cleavage cracking characteristic. The upper region was the LAS transition layer, and the 309L was located in the bottom region, as shown in Fig. 21(a). The fracture morphology of the LAS transition layer was smoother than that of the A508III base metal, and no significant necking occurred in the specimen. The fracture mode of the LAS transition layer displayed a ductile-dominated mixed-mode fracture with quasi-cleavage crack regions and some secondary cracks, as shown in Figs. 21(b) and (d). The bottom 309L portion exhibited brittle fracture features, as evidenced by the amounts of tearing-like cracks distributed on the fracture surface. Many holes were observed on the 309L fracture surface due to the decohesion of the inclusions from base metal, as shown in Figs. 21(c), (e) and (f).

Figure 22 shows the stress-strain curves after SSRT at 3×10^{-7}/s and 1×10^{-6}/s for 309L/308L specimens in hydrogenated simulated PWR primary water at 325 ºC. The elongation to failure, YS and UTS for 309L/308L specimen after SSRT at 3×10^{-7}/s in hydrogenated primary water were 40.8%, 235 MPa and 402 MPa, respectively. The elongation to failure, YS and UTS for 309L/308L specimen after SSRT at 1×10^{-6}/s in hydrogenated primary water was 36.3%, 245 MPa and 432 MPa, respectively.

Figure 23 shows the fracture surface and gauge length side morphologies of 309L/308L specimen after SSRT at 3×10^{-7}/s in hydrogenated simulated PWR primary water at 325 ℃. Some brittle and tearing-like cracking regions were observed at the 309L side, especially on the right edges (near the FB), suggesting that local SCC had occurred in these regions, as shown in

Figs. 23(a_2) and (a_3). The fracture surface for 308L (left part) displayed ductile features, as shown in Fig. 23(a_1). It was apparent that some large transgranular (TG) cracks were present on the gauge side surface of 309L (right part) in Figs. 23(b_2) and (b_3). The transgranular cracks on the gauge side surface of 308L (left part) could not be clearly observed at low magnification and required a higher magnification, as shown in Fig. 23(b_1). The number of oxide particles on 309L side was more than that on the 308L side, as shown in Figs. 23(b_1-b_3).

Figure 24 shows the fracture surface and gauge length side morphologies of 309L/308L specimen after SSRT at 1×10^{-6}/s in simulated normal PWR primary water at 325 ℃. The fracture surface contains two parts, the left portion for the 309L and the right portion for the 308L. The edge of the 309L portion has some tearing-like cracking regions, as shown in Figs. 24(a_2) and (a_3), which are less significant than similar ones in 309L/308L after SSRT at 3×10^{-7}/s in hydrogenated primary water of PWR. The tensile fracture in 308L side (right portion) exhibited a ductile shear-dominated mixed-mode fracture with dimple-like fracture and quasi-cleavage regions, as shown in Fig. 24(a_1). No obvious tensile deformation appears on the gauge side surface of 309L (left part), and some transgranular cracks are observed on the 309L part, as shown in Figs. 24(b_2) and (b_3). Some deformation regions with small transgranular cracks on the gauge side surface of 308L (right part) were observed, as shown in Fig. 24(b_1). The oxide particles on 309L side were more and larger in size than those on 308L side, as shown in Figs. 24(b_1-b_3).

4. Discussion

4.1. Effect of composition and microstructure on oxidation of SS claddings

The double-layer structure oxide film formation could be related to the following reasons. The Cr has the largest diffusion coefficient in the fcc Fe-Cr-Ni lattice and the highest reactivity to oxygen [32,33], which resulted in the preferential oxidation of Cr during the initial oxidation process. After prolonging the oxidation period, some Fe and Ni would dissolve and diffuse through the Cr-rich oxide and react with Cr oxide to form $Cr_xFe_yNi_zO_4$; the other Fe and Ni would transport through the internal oxide film to form the external oxide [34]. Ni was always accumulated at the oxide/matrix interface due to its lowest affinity to oxygen and the lowest diffusion rate in the metal substrate [24,32]. Preferential oxidation of deformation/slip bands and grain boundaries was observed in this study is shown in Fig. 15 and Fig. 18, respectively. It

was reported that the grain boundaries and deformation bands show enhanced oxidation due to these regions having a high defect density and acting as fast diffusion paths [35,36]. The role of Cr-rich intergranular carbides in grain boundary oxidation and SCC of a cold-worked alloy 600 has been discussed by Shen et al. [37]. Intergranular carbides are thermodynamically stable during the oxidation process. Intergranular carbides provide Cr to favor protective Cr-rich oxide formation to prevent the oxidation along the grain boundaries and improve cracking resistance after prior cold-work [37]. Persaud et al. [38] reported an "oxygen sink" mechanism to elucidate the intergranular carbides mitigating effect on the oxidized grain boundary in high-temperature hydrogenated steam. The "oxygen sink" mechanism assumed the intergranular carbides to be more readily oxidized by the inward transport of oxygen, thereby preventing further intergranular oxygen diffusion [38].

It was reported that the chemical composition, such as Cr content in the substrate [35,39−41], plays an essential role in the oxidation resistance of austenitic alloys. Increasing Cr content in the alloy reduces the corrosion rate [39] or decreases the thickness of the corrosion products [40] in hydrogen-bearing primary water media. Arioka and co-workers research shows that Cr content in austenitic SS significantly affects the CGR in PWR primary water environment [41]. The initial Cr content is related to how protective surface oxide will be (Cr_2O_3 will form if enough Cr is available and then Cr-rich spinel) during oxidation in high-temperature water, which can be illustrated by Alloy 690 having much higher oxidation and SCC resistance than Alloy 600 [42,43]. If the amount of available trivalent cations (mainly Cr^{3+}) is not enough, Cr-rich spinel will form, but with defects and a high voids density [44]. The inner oxide film contained ~17% at. Cr on 309L, and ~20% at. on 308L. The formation of Cr_2O_3 requires 40% at. Cr, and $FeCr_2O_4$/$NiCr_2O_4$ require ~29% at. [45], neither 309L nor 308L can provide sufficient Cr to form a continuous compact and protective oxide, as shown in Figs. 15−18. However, it can be concluded that an initial higher Cr content in the matrix favors the formation of a more protective surface oxide. The Cr content in 309L is lower than that in 308L, resulting in a thicker oxide layer with many voids formed on 309L.

The oxidation resistance of 308L SS in simulated PWR primary water was higher than that of 309L SS. Besides the Cr content discussed above, the ferrite in the stainless steel weld metals also significantly affects oxidation resistance in high-temperature water. Some researchers

suggested that the ferrite can act as a Cr source to form the protective oxide film during high-temperature water exposure [24,46]. Due to the open lattice structure of the ferrite phase, the metal transport in the ferrite phase is faster than that in the austenite phase (close lattice structure) [47−49]. The δ-ferrite has higher Cr content than austenite, as verified by SEM-EDS, as shown in Fig. 11(c). A much lower volume fraction and network-level of ferrite in 309L SS than that in 308L SS (as shown in Figs. 9(b)-(d), and 11 (a) and (b)), resulted in a higher oxidation rate of 309L SS than that of 308L SS in hydrogen-bearing PWR primary water.

4.2. Effect of microstructure on mechanical property and SCC performance

The higher YS and tensile strength in the A508III transition layer than that in bulk metal could be related to a large number of carbides ($M_{23}C_6$) precipitating. The complex microstructure of the transition layer due to weld heat-affected is associated with carbon-depleted; therefore, it decreases the elongation rate to failure. The highest hardness in the fusion boundary zone could be related to the presence of a martensitic layer. It was reported that the lattice structure of martensite tends to change from body-centered tetragonal to hexagonal with increases in the carbon content [50], which is consistent with the EPMA carbon-mapping shown in Fig. 7.

It was reported that high-angle boundaries are more susceptible to cracking than low-angle and coincidence-site-lattice boundaries [51]. The type-I and type-II boundaries were high-angle boundaries and had relatively lower resistance to crack growth than FB [6,52,53]. 309L has higher strength than 308L, as reported in previous work [54]. The high strength/hardness of 309L SS would be due to the high-density dislocations and residual stress/strain caused by welding; these tend to decrease SCC resistance in simulated primary water. The higher strength causes elastic strain energy to increase in the vicinity of the crack-tip, thereby increasing the driving force for intergranular crack growth [35]. Bulloch [55] studied the influence of material yield strength on the threshold SCC of low alloy steels in various aqueous environments at ambient temperatures, found that the fracture mode changed from transgranular to intergranular with increases in yield strength. The threshold stress intensity of SCC, K_{ISCC} value was strongly influenced by material strength, which can be expressed by the following equation [55]

$$K_{ISCC} = 6 \times 10^{9} (\sigma_y)^{-2.6514} \quad (1)$$

where σ_y represent the materials yield strength.

As discussed above, preferential oxidation of slip bands in 309L would provide preferential and fast oxygen diffusion paths, increasing the SCC susceptibility. Sinjlawi et al. [56] observed oxidation and crack branching along slip bands, suggesting that slip bands provide more accessible diffusion paths for oxygen, resulting in preferential oxidation and crack propagation. Slip bands were responsible for oxide film rupture due to the high local dislocation density in these regions. The large amounts of δ-ferrite in 308L SS weld would improve the resistance to SCC. Wang et al. [46] found that the scattered δ-ferrite contributed to crack branching formation and reduced the stress intensity factor *K* at the crack tips, thus decreasing the SCC CGR. Abe et al. [57] have studied the SCC performance near the FB of a 316NG SS welded joint in 288 ℃ high-purity water, found that the CGR at the δ-γ boundary was calculated about 0.957 times of the γ-γ boundary. High Cr content and the δ-ferrite microstructure improve the corrosion resistance, causing the SCC retardation. Lu et al. [58] observed that CGRs of 316NG weld metals were strongly dependent on the ferrite percentage, and CGRs are higher in the low ferrite (6.5% wt.) weld metal versus the high ferrite (8.5% wt.) weld metal at the same experiment condition. The SCC growth mainly along the δ-γ phase boundaries of 316L SS weld, accompanied by preferential corrosion appearing in the austenite phase versus the ferrite phase [59]. Krishnan et al. [60] reported that δ-ferrite morphology could influence the SCC performance of austenitic SS welds and discontinuous network ferrite in austenite substrate displayed a better SCC resistance. The oxidation resistance of 309L SS is lower than that of 308L SS in the normal PWR primary water. The reported results for the microstructure, material chemistry and oxidation resistance are consistent with the fracture mode observed in 308L SS and 309L SS cladding layers.

5. Conclusions

Microstructures and oxide films of 308L SS and 309L SS cladding layers have been characterized and compared. The SCC susceptibility of A508III-309L/308L SS cladding layers in simulated PWR primary water was investigated by SSRT tests, finding that:

(1) The HAZ in the A508III side has a complex microstructure consisting of a coarse-grained zone (carbon-depleted zone) and a fine-grained zone. The existence of a lath martensitic layer in the fusion zone increases the hardness adjacent to the FB.

(2) A double-layer structure oxide grown on 308L SS and 309L SS, with Fe-rich oxide particles in the external layer and Cr-rich fine crystals in the internal layer. Ni was accumulated at the oxide/matrix boundary with Fe-Cr-depletion. The oxidation resistance of 308L SS superior to that of 309L SS, mainly due to the higher Cr-content and network-level of δ-ferrite in 308L after welding.

(3) Preferential oxidation of slip bands would provide a preferential and fast oxygen diffusion path, decrease the oxidation resistance of 309L SS. Intergranular carbides provide Cr to favor protective Cr-rich oxide formation to inhibit further oxidation along the grain boundaries.

(4) Large amounts of carbides precipitation, complex microstructure and high residual stress/strain in the HAZ are responsible for the high hardness and strength in the A508III transition layer.

(5) The presence of type-I and type-II boundaries, composition dilution, and less δ-ferrite content synergistically contribute to increasing the SCC susceptibility of 309L SS cladding in simulated PWR primary water.

Acknowledgements

This work has been supported by National Key R&D Program of China (No. 2017YFB0703002), Natural Science Foundation of China (NSFC No. 51771107), National Science and Technology Major Project No. 2015ZX06002005.

Reference

[1] X. Y. Cao, P. Zhu, T. G. Liu, Y. H. Lu, T. Shoji, Surf. Coat. Tech. 344(2018) 111−120.

[2] J. Chen, C. Jang, B. S. Kong, Q. Xiao, G. Obulan Subramanian, H. S. Kim, J. H. Shin, Corros. Sci. 172(2020) 108730.

[3] H. Ming, Z. Zhang, J. Wang, R. Zhu, J. Ding, J. Wang, E. H. Han, W. Ke, Appl. Surf. Sci. 337(2015) 81−89.

[4] K. Chandra, V. Kain, V. S. Raja, R. Tewari, G. K. Dey, Corros. Sci. 54(2012) 278−290.

[5] X. Y. Cao, P. Zhu, X. F. Ding, Y. H. Lu, T. Shoji, J. Nucl. Mater. 486(2017) 172−182.

[6] H. Ming, Z. Zhang, J. Wang, E. H. Han, W. Ke, Mater. Charact. 97(2014) 101−115.

[7] Howell AT. Davis–Besse reactor vessel head degradation lessons learned task force report. US Nuclear Regulatory Commission 2002.

[8] G.F. Li, W. Yang, Nucl. Saf. 2 (2003) 37−40.

[9] G. F. Li, J. Congleton, Corros. Sci. 42 (2000) 1005−1021.

[10] G. F. Li, Y. F. Yuan, X. Lu, Procedia Engineering. 130(2015) 1572−1579.
[11] W.C. Chung, J.Y. Huang, L.W. Tsay, C. Chen, J. Nucl. Mater. 408 (2011) 125−128.
[12] G. F. Li, E. A. Charles, J. Congleton, Corros. Sci. 43 (2001) 1963−1983.
[13] I. Hamada, K. Yamauchi, Nucl. Eng. Des. 214(2002) 205−220.
[14] Z. Lu, T. Shoji, Y. Takeda, Y. Ito, A. Kai, N. Tsuchiya, Corros. Sci. 50(3) (2008) 625−638.
[15] T. Takeuchi, Y. Kakubo, Y. Matsukawa, Y. Nozawa, T. Toyama, Y. Nagai, Y. Nishiyama, J. Katsuyama, Y. Yamaguchi, K. Onizawa, M. Suzuki, J. Nucl. Mater. 452 (2014) 235−240.
[16] T. Takeuchi, J. Kameda, Y. Nagai, T. Toyama, Y. Matsukawa, Y. Nishiyama, K. Onizawa, J. Nucl. Mater. 425 (1-3) (2012) 60−64.
[17] T. Takeuchi, J. Kameda, Y. Nagai, T. Toyama, Y. Nishiyama, K. Onizawa, J. Nucl. Mater. 415(2) (2011) 198−204.
[18] J. A. Brooks, A. W. Thompson, Int. Mater. Rev. 36(1) (1991) 16−44.
[19] Y. S. Lim, S. S. Hwang, S. W. Kim, H. P. Kim, Corros. Sci. 100(2015) 12−22.
[20] Z. Lu, T. Shoji, F. Meng, H. Xue, Y. Qiu, Y. Takeda, K. Negishi, Corros. Sci. 53(5)(2011) 1916−1932.
[21] M. L. Zhang, Y. H. Lu, S. H Chen, L. J. Rong, H. Lu, Acta Metall. Sin. 56(8) (2020) 1057−1066.
[22] T. R. Beck, Corrosion 30 (1974) 408−414.
[23] J. C. Scully, Corros. Sci. 8 (1968) 759−769.
[24] Q. Xiong, H. J. Li, Z. P. Lu, J. J. Chen, Q. Xiao, J. R. Ma, X. K. Ru, J. Nucl. Mater. 498 (2018) 227−240.
[25] Q. Xiong, J. R. Ma, T. M. Cui, K. Zhang, Z. P. Lu, J. J. Chen, Y. B. Jia, Characteristics of oxide films formed on 309L and 308L stainless steels in simulated PWR primary water, in: Proc. 19th Int. Conf. Environ. Degradation of Materials in Nuclear Power Systems-Water Reactors, Boston, MA, August 18-22, (2019) 824−837.
[26] T. M. Cui, F. Ning, J. R. Ma, Z. P. Lu, K. Zhang, Y. B. Jia, X. Liang, X. K. Ru, T. Shoji, Local oxidation penetration of hydrogen-charged 308L stainless steel cladding in deaerated PWR primary water, in: Proc. 19th Int. Conf. Environ. Degradation of Materials in Nuclear Power Systems-Water Reactors, Boston, MA, August 18-22, (2019) 750−764.
[27] M. Henthorne, Corrosion 72(12) (2016) 1488−1518.
[28] S. Wang, Y. Hu, K. Fang, W. Zhang, X. Wang, Corros. Sci. 126(2017) 104−120.
[29] F. Mas, C. Tassin, N. Valle, F. Robaut, F. Charlot, M. Yescas, F. Roch, P. Todeschini, Y. Bréchet, J. Mater. Sci. 51(10) (2016) 4864−4879.
[30] R. P. Matthews, R. D. Knusten, J. E. Westraadt, T. Couvant, Corros. Sci. 125(2017) 175−183.
[31] Z. Que, M. Heczko, I. Kuběna, H. P. Seifert, P. Spätig, Mater. Charact. 165(2020) 110405
[32] J. J. Chen, Z. P. Lu, F. J. Meng, X. L. Xu, Q. Xiao, H. S. Kim, C. Jang, J. Nucl. Mater. 517 (2019) 179−191.
[33] S. J. Rothman, L. J. Nowicki, G. E. Murch, J. Phys. F Met. Phys. 10(3) (1980) 383−398.
[34] E. L. Shock, H. C. Helgeson, Geochim. Cosmochim. Acta 52 (1988) 2009−2036.
[35] S. Lozano-Perez, T. Yamada, T. Terachi, M. Schröder, C. A. English, G. D. W. Smith, C. R. M. Grovenor, B. L. Eyre, Acta Mater. 57(18) (2009) 5361−5381.
[36] S. Lozano-Perez, K. Kruska, I. Iyengar, T. Terachi, T. Yamada, Corros. Sci. 56 (2012) 78−85.

[37] Z. Shen, J. Dohr, S. Lozano-Perez, Corros. Sci. 155(2019) 209−216.
[38] S. Y. Persaud, A. Korinek, J. Huang, G. A. Botton, R. C. Newman, Corros. Sci. 86 (2014) 108−122.
[39] T. Terachi, T. Yamada, T. Miyamoto, K. Arioka, K. Fukuya, J. Nucl. Sci. Technol. 45(10) (2008) 975−984.
[40] K. Arioka, T. Yamada, T. Terachi, R. W. Staehle, Corrosion 62(1) (2006) 74−83.
[41] K. Arioka, T. Yamada, T. Terachi, G. Chiba, Corrosion 62(7) (2006) 568−575.
[42] K. Arioka, T. Yamada, T. Miyamoto, T. Terachi, Corrosion 67(3) (2011) 035006-1−18.
[43] J. B. Ferguson, H. F. Lopez, Metall. Mater. Trans. 37(2006) 2471−2479.
[44] S. M. Bruemmer, B. W. Arey, L. A. Charlot, Corrosion 48(1992) 42−49.
[45] Z. Shen, M. Meisnar, K. Arioka, S. Lozano-Perez, Acta Mater. 165(2019) 73−86.
[46] J. Wang, H. Su, K. Chen, D. Du, L. Zhang, Z. Shen, Corros. Sci. 158(2019) 108079.
[47] R. N. Gunn, Duplex Stainless Steels: Microstructure, Properties and Applications, 6-Corrosion, Woodhead Publishing, (1997) 73−91.
[48] P. Williams, R. Faulkner, J. Mater. Sci. 22(10) (1987) 3537−3542.
[49] M. A. E. Jepson, R. L. Higginson, Corros. Sci. 59(2012) 263−269.
[50] V. Olden, C. Thaulow, R. Johnsen, Mater. Des. 29(10) (2008) 1934−1948.
[51] S. M. Bruemmer, in: C.A. Schuh, M. Kumar, V. Randle, C.B. Carter (Eds.), MRS Symposium Proceeding vol. 819, (2004) N2.2.1−N2.2.10.
[52] T. W. Nelson, J. C. Lippold, M. J. Mills, Weld. J. 78(1999) 329s−337s.
[53] T. W. Nelson, J. C. Lippold, M. J. Mills, Weld. J. 79(2000) 267s−277s.
[54] Q. Xiong, T. M. Cui, J. R. Ma, Z. P. Lu, F. Ning, J. J. Chen, K. Zhang, Z. M. Zhong, G. D. Han, Stress corrosion cracking of stainless steel cladding layers in simulated PWR primary water, in: Proc. 19th International Conference on Environmental Degradation of Materials in Nuclear Power System-Water Reactors, Boston, MA, August 18-22, (2019) 1095−1102.
[55] J. H. Bulloch, Eng. Fail. Anal. 11 (2004) 843−856.
[56] A. Sinjlawi, J. J. Chen, H. S. Kim, H. B. Lee, C. Jang, S. Lee, Nucl. Eng. Technol. 52(11) (2020) 2552−2564.
[57] H. Abe, Y. Watanabe, J. Nucl. Mater. 424(1-3) (2012) 57−61.
[58] Z. P. Lu, T. Shoji, Y. Takeda, Corros. Eng. Sci. Technol. 50 (2014) 41−48.
[59] D. J. Edwards, L. E. Thomas, K. Asano, S. Ooki, S. M. Bruemmer, Microstructure, microchemistry and stress corrosion crack characteristics in a BWR 316L SS core shroud weld, in: Proceeding of 13th International Conference on Environmental Degradation of Materials in Nuclear Power Systems–Water Reactors, CNS, 2007.
[60] K. N. Krishnan, K. P. Rao, Mater. Sci. Eng. A142 (1991) 79−85.

Figure captions

specimen in simulated PWR primary water at 325 °C.

Fig. 24. SEM morphologies of the fracture surface and gauge side after SSRT at 1×10^{-6}/s for 309L/308L specimen in simulated PWR primary water at 325 °C.

Table captions

Table 1

Chemical compositions of the LAS matrix and the SS cladding layers (wt. %).

Table 2

Summary of the mechanical properties of the A508III-309L/308L SS cladding layers after SSRT tests at different strain rates.

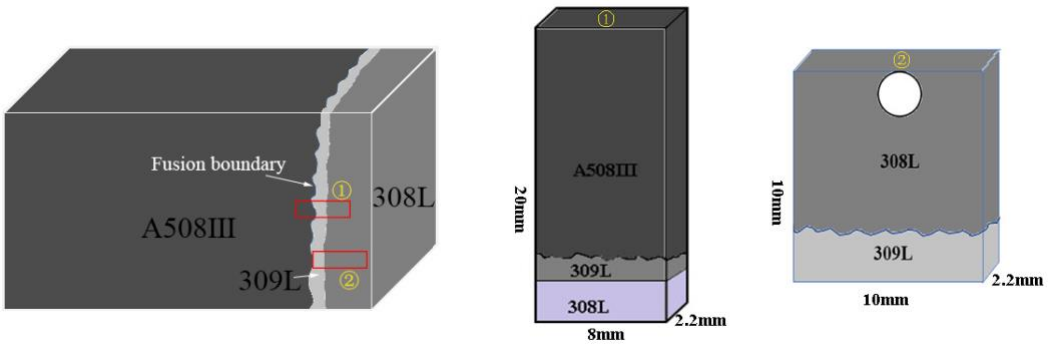

Fig. 1. Sampling location of A508III-309L/308L SS cladding: red box 1 for microhardness and metallographic sample, red box 2 for exposure sample.

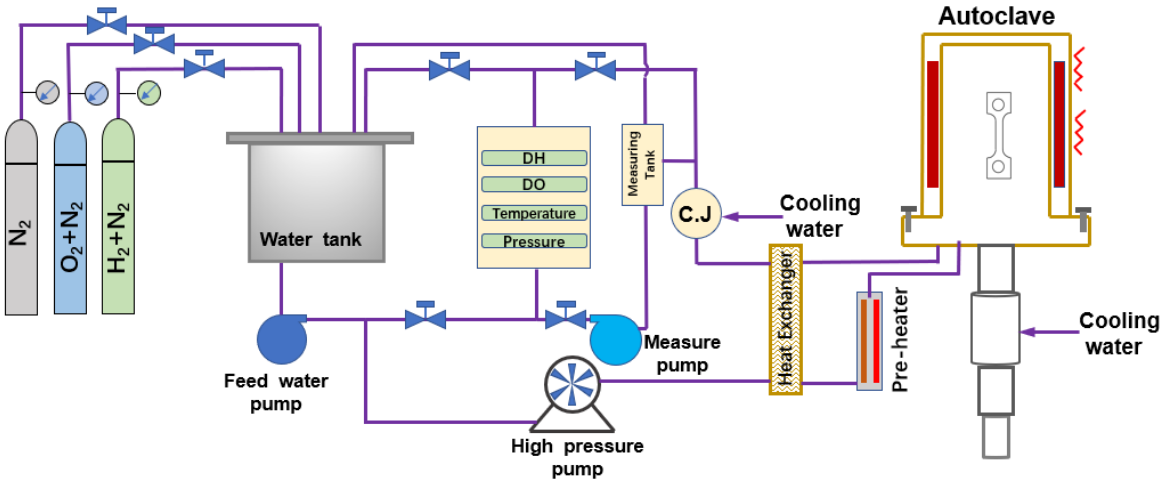

Fig. 2. Schematic of a 316 SS autoclave equipped with water re-circulating loop system for exposure and SSRT tests.

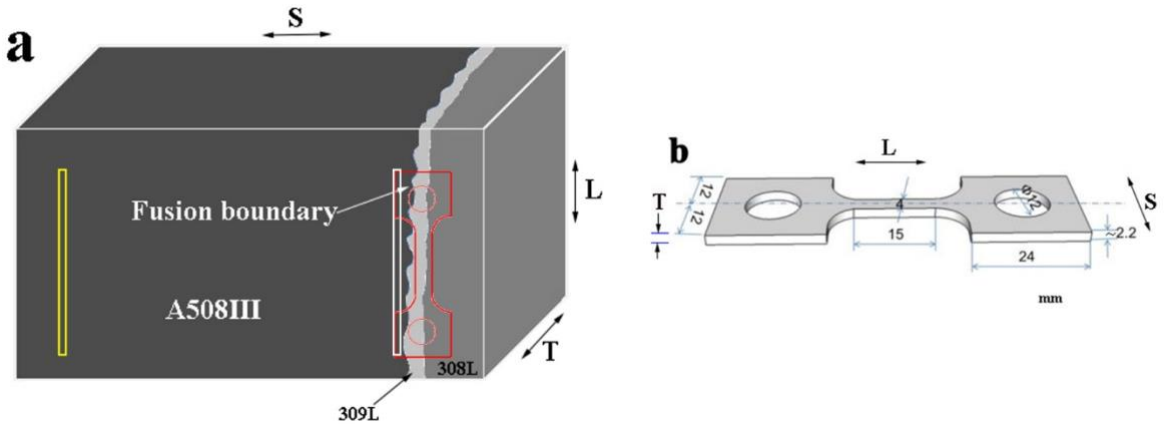

Fig. 3. (a) Schematic of the locations for taking the SSRT specimens, (b) the SSRT specimen size.

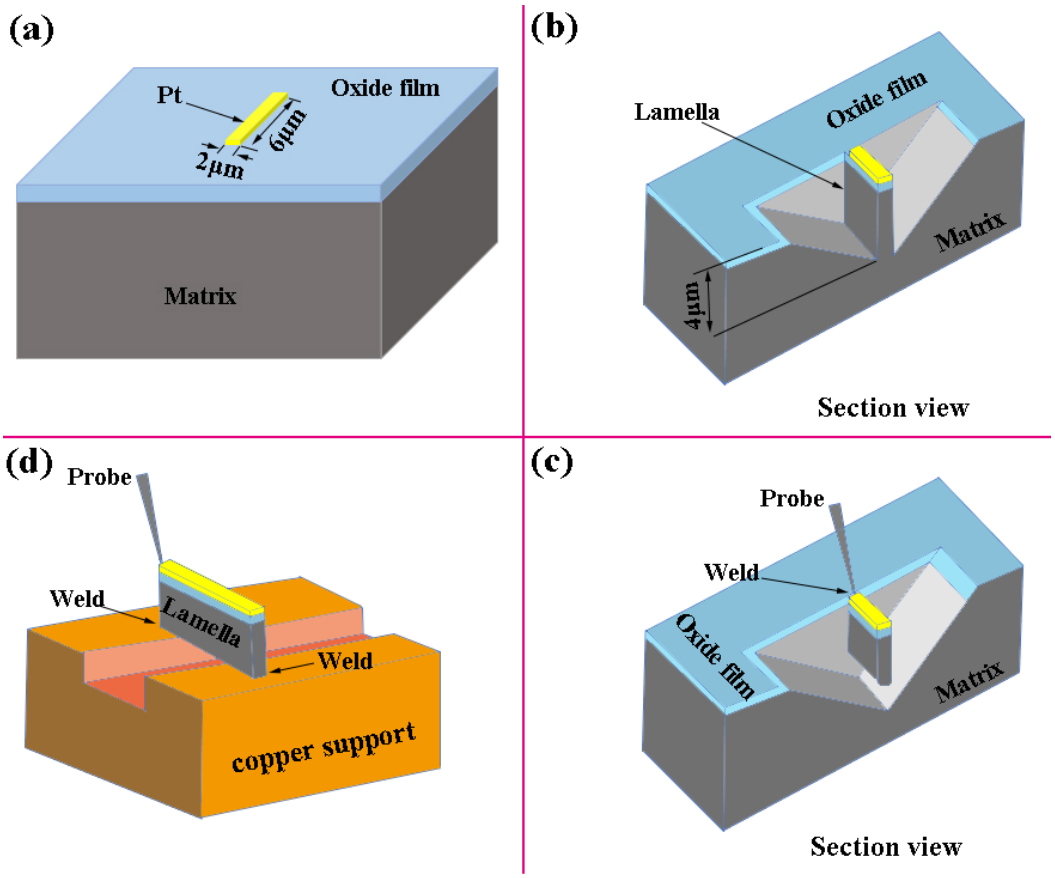

Fig. 4. Schematic of the process for preparing TEM foil specimens by a FIB system [26].

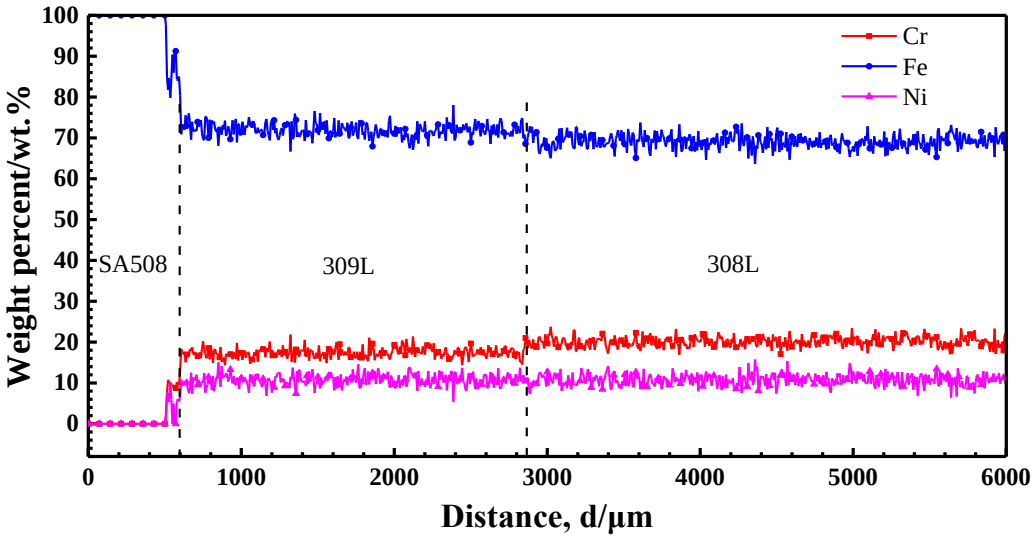

Fig. 5. SEM-EDS results of elements distribution of the A508III-309L/308L.

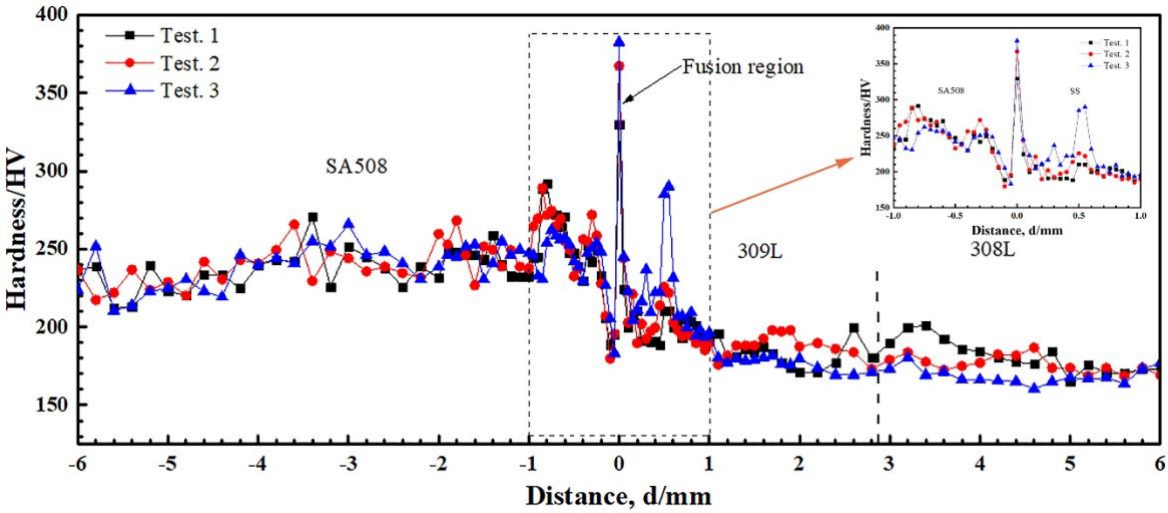

Fig. 6. Microhardness profiles of the A508III-309L/308L SS cladding from multiple measurements.

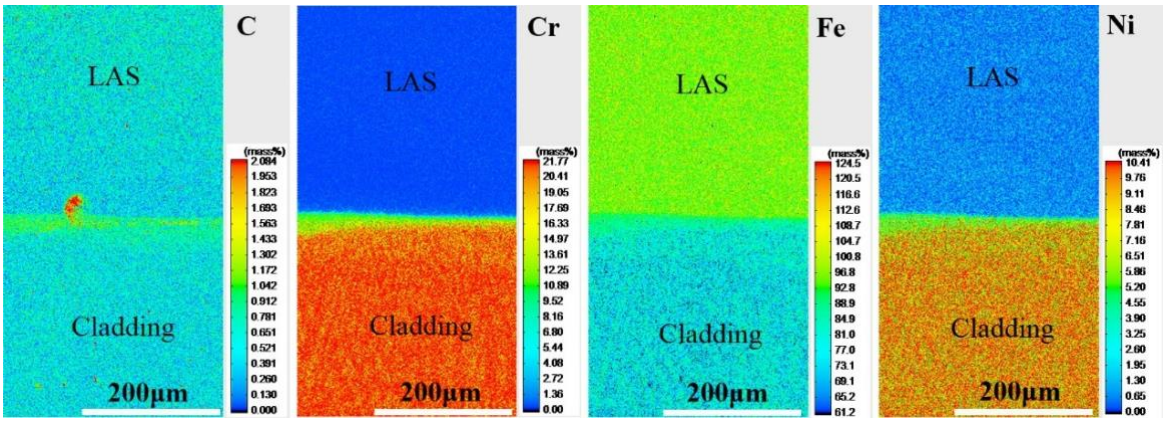

Fig. 7. EPMA maps of C, Fe, Cr and Ni distribution near fusion line of A508III-309L/308L SS cladding.

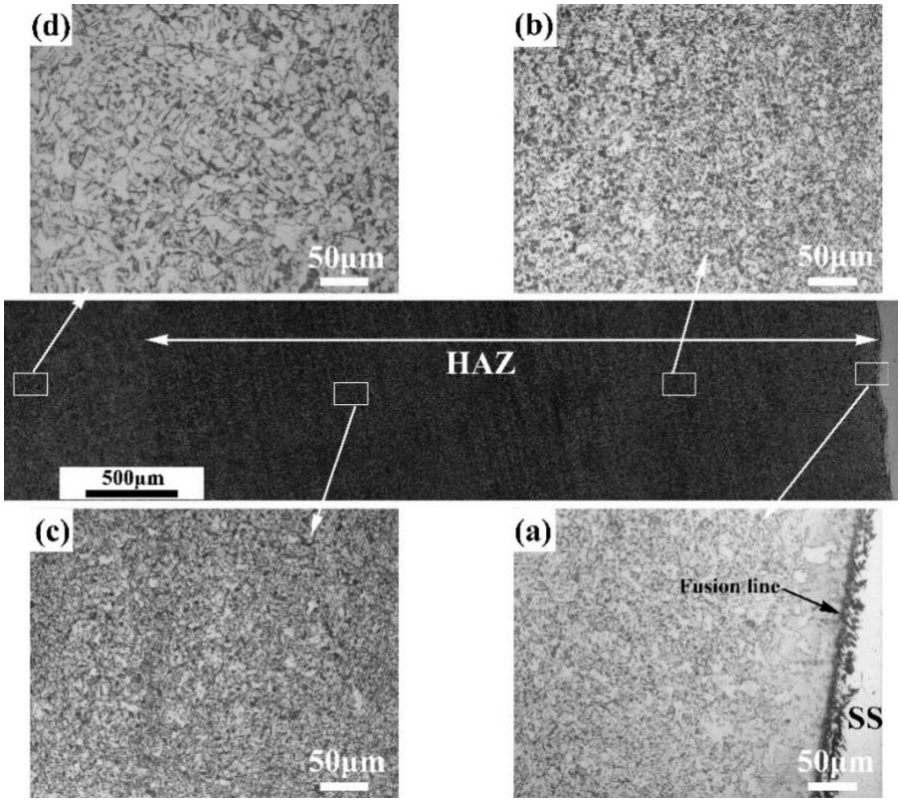

Fig. 8. Metallographic structures of A508III: (a)-(c) Heat-affected zone, (d) A508III base metal.

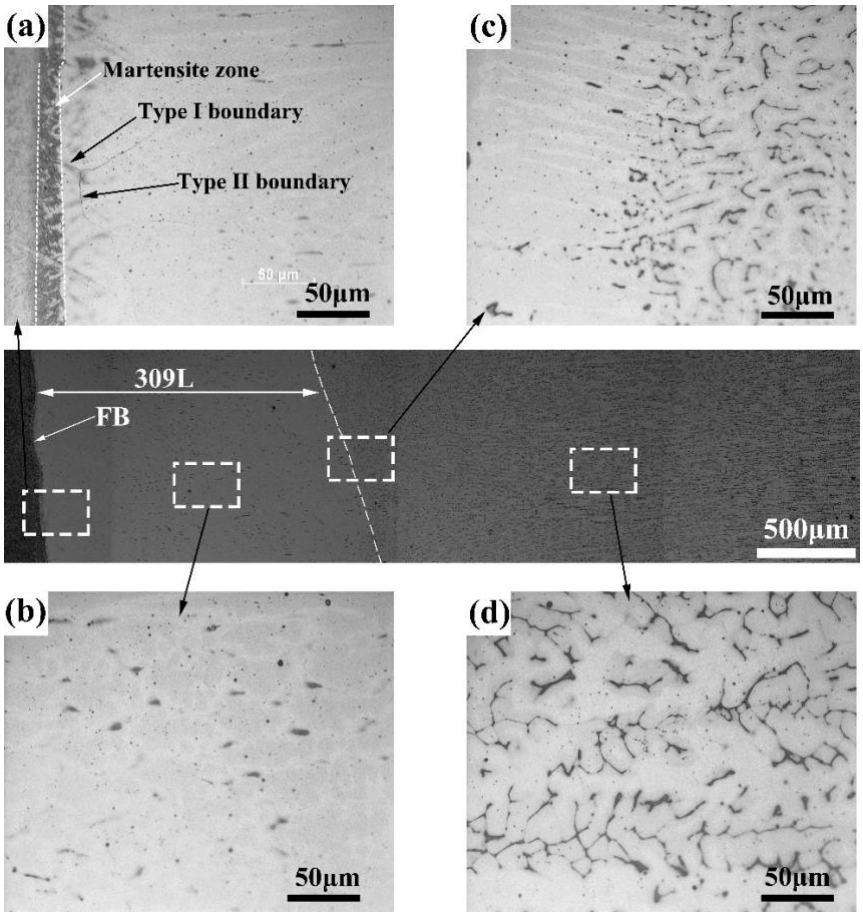

Fig. 9. Metallographic structures of 309L/308L SS cladding layers: (a) the interface of A508III-309L, (b) 309L matrix, (c) the interface of 309L/308L, (d) 308L matrix.

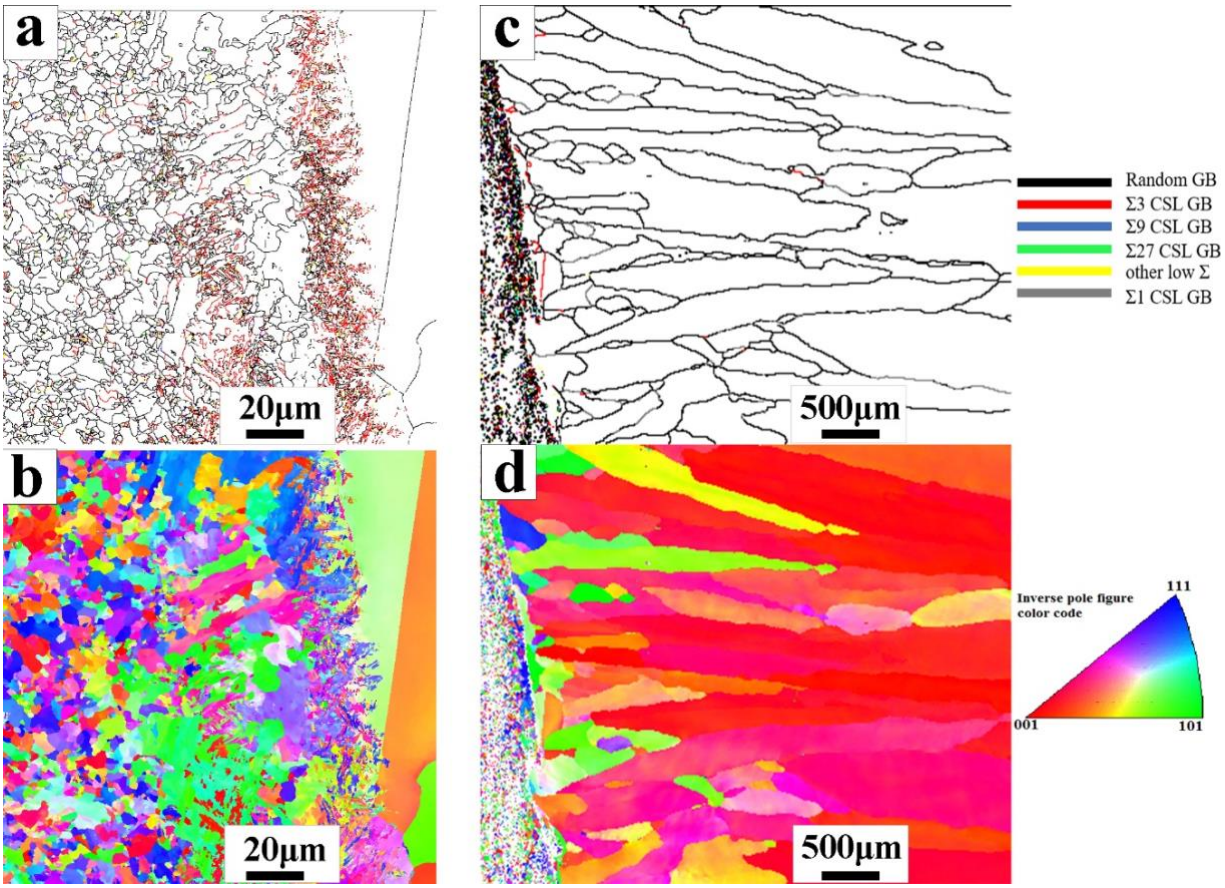

Fig. 10. EBSD results of A508III and 309L SS near the FB: (a) Grain boundary types of the LAS near the FB, (b) IPF of the LAS near the FB, (c) Grain boundary types of the 309L SS near the FB, (d) IPF of the 309L SS near the FB.

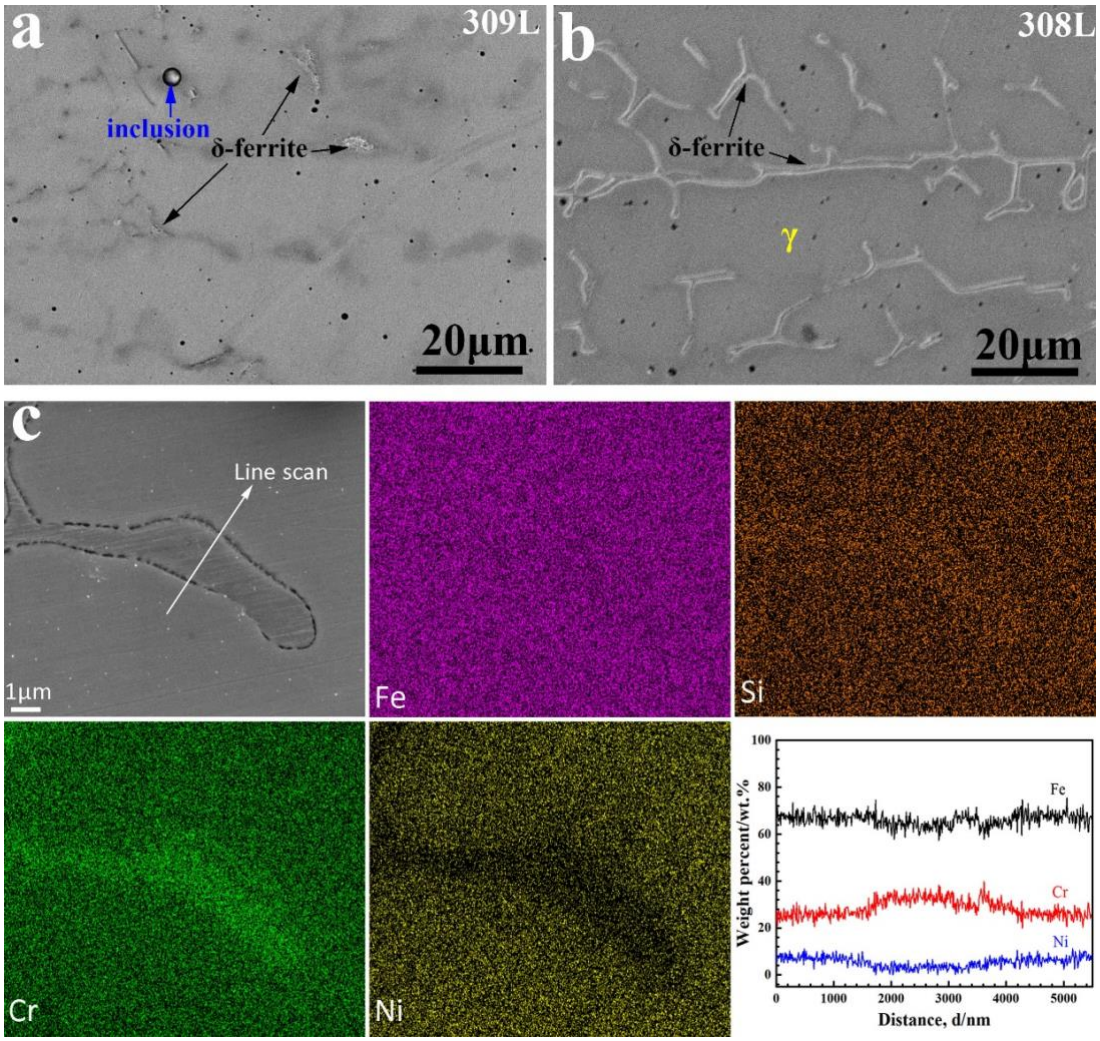

Fig. 11. (a) SEM morphology of ferrites in 309L SS, and (b) SEM morphology of ferrites in 308L SS, (c) SEM-EDS area maps and the element profile of the ferrite.

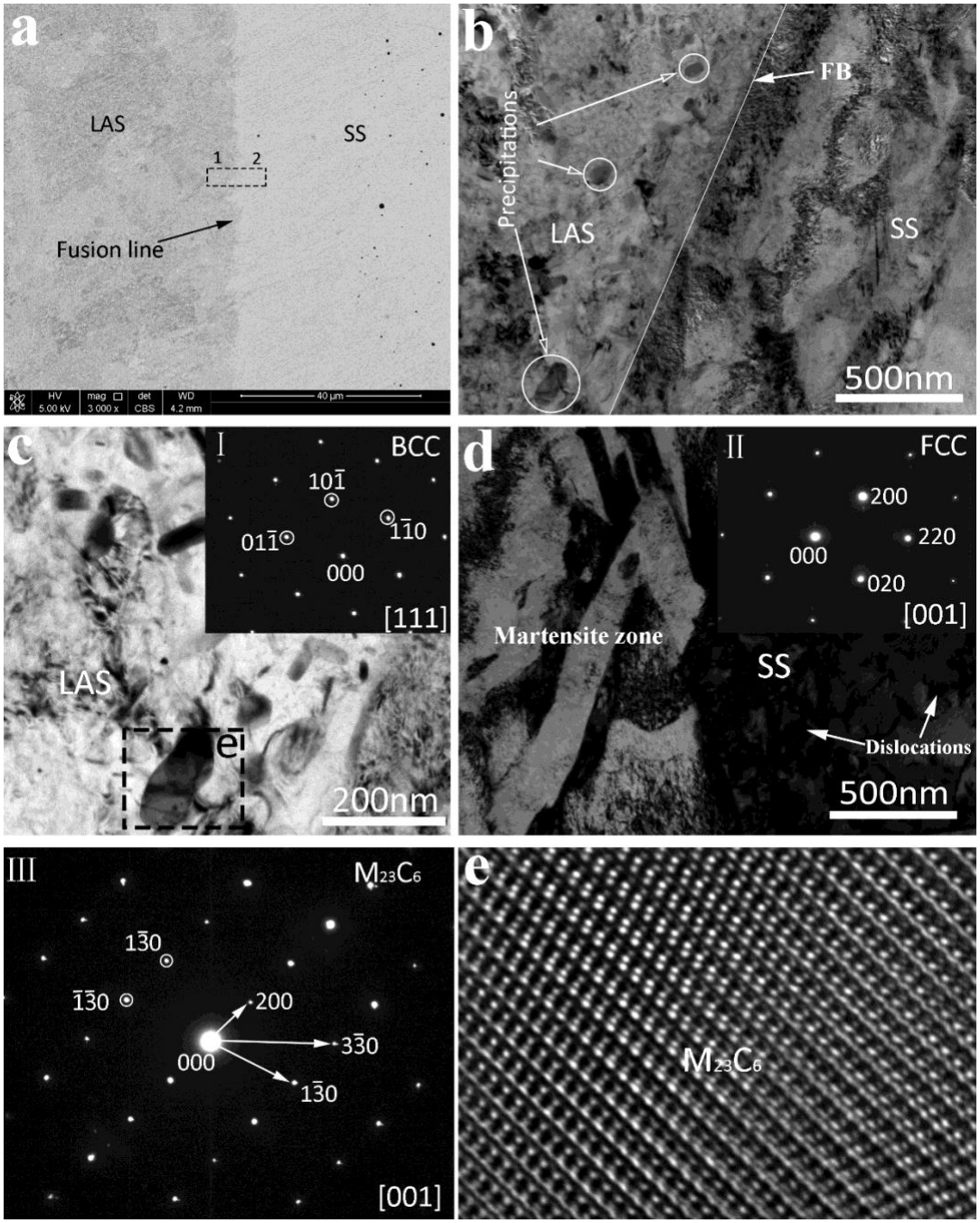

Fig. 12. (a) A508III-309L interface and TEM sampling location, (b) High resolution TEM image of the A508III-309L interface, (c) TEM-BF image of the A508III transition zone, (d) TEM-BF image of the 309L side near the FB, (e) High resolution TEM image of the carbide in A508III. (I) SAED pattern of the A508III matrix, (II) SAED pattern of the 309L SS matrix, (III) SAED pattern of the carbides.

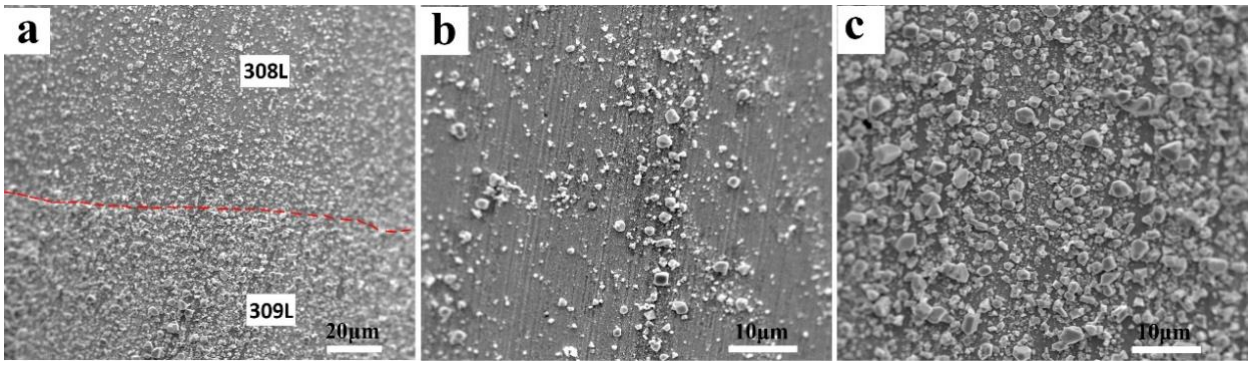

Fig. 13. SEM morphologies of oxide films after exposure to simulated PWR primary water at 325 ºC for 500 h. (a) 309L/308L SS interface, (b) 308L SS, (c) 309L SS.

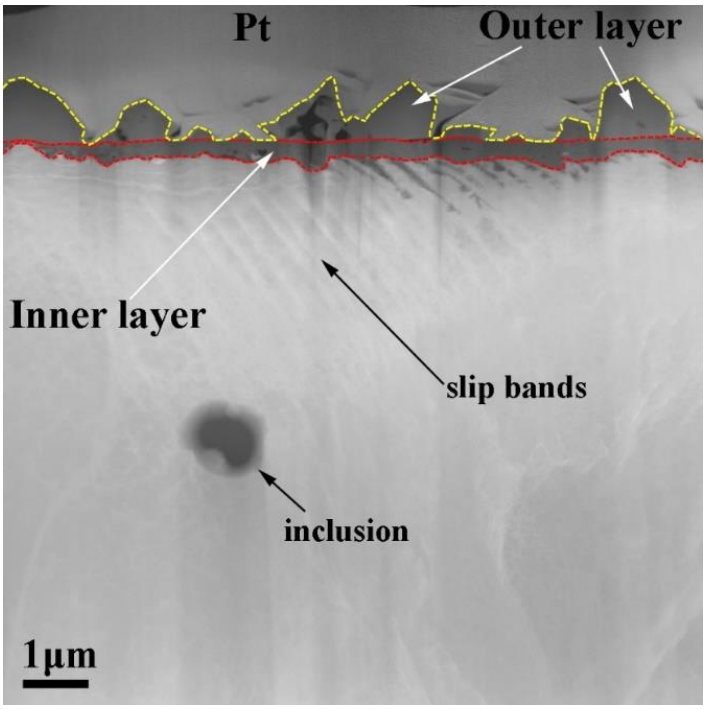

Fig. 14. Low magnification STEM-HAADF image of the oxide film formed on 309L SS after exposure to simulated PWR primary water at 325 ºC for 500 h.

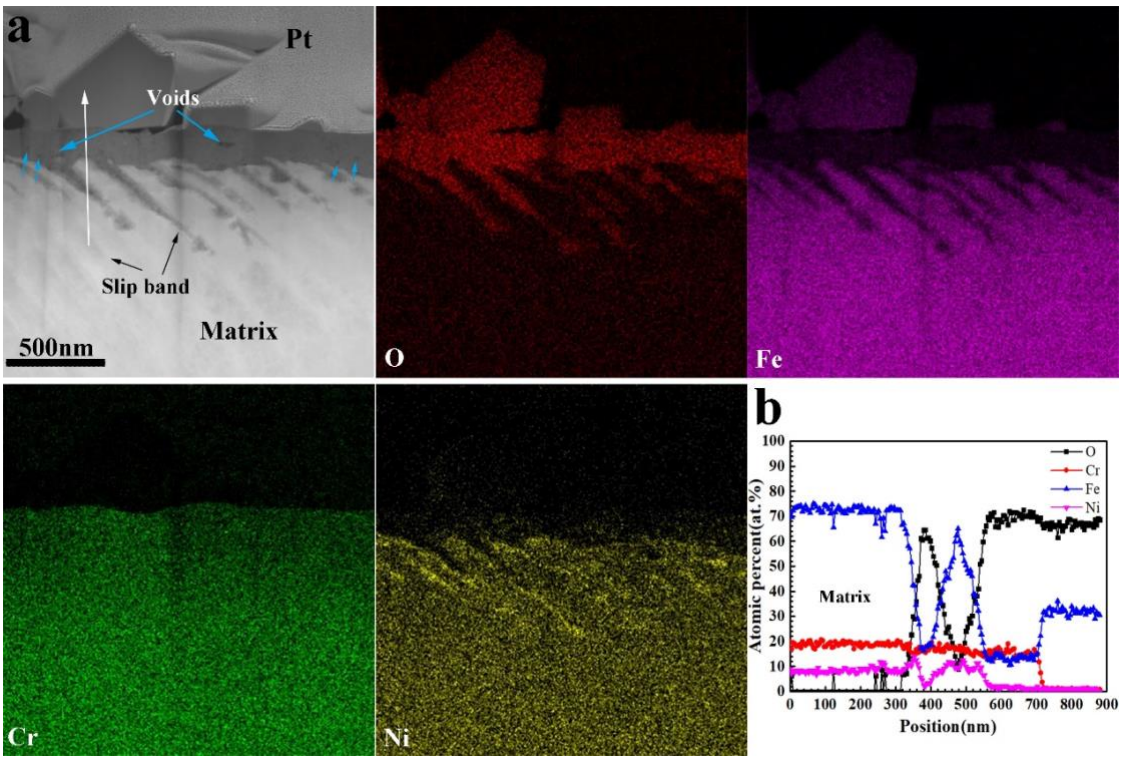

Fig. 15. (a) High magnification STEM-HAADF image of the oxide film (selection-area 1) formed on 309L SS and the corresponding EDS maps, (b) EDS line scan profile of the oxide film shown in (a).

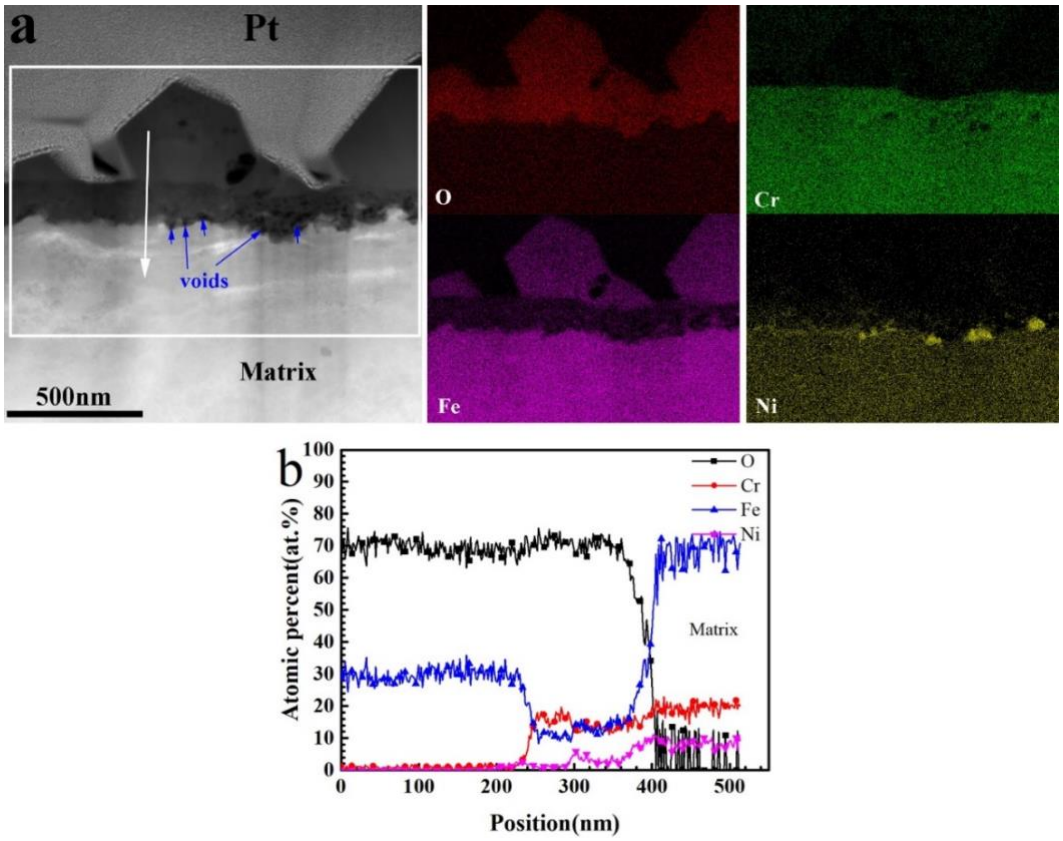

Fig. 16. (a) High magnification STEM-HAADF image of the oxide film (selection-area 2) formed on 309L SS and the corresponding EDS maps, (b) EDS line scan profile of the oxide film shown in (a).

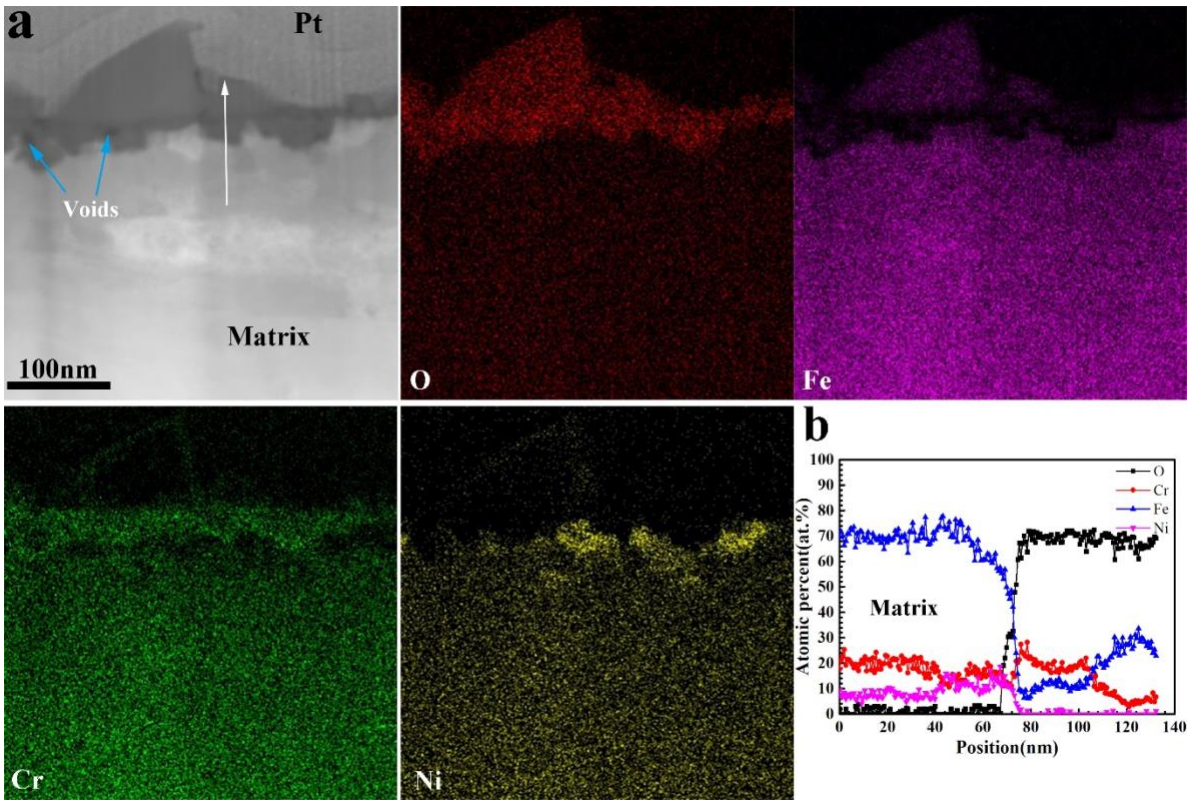

Fig. 17. (a) STEM-HAADF image of the oxide film formed on 308L SS and the corresponding EDS maps, (b) EDS line scan profile of the oxide film shown in (a).

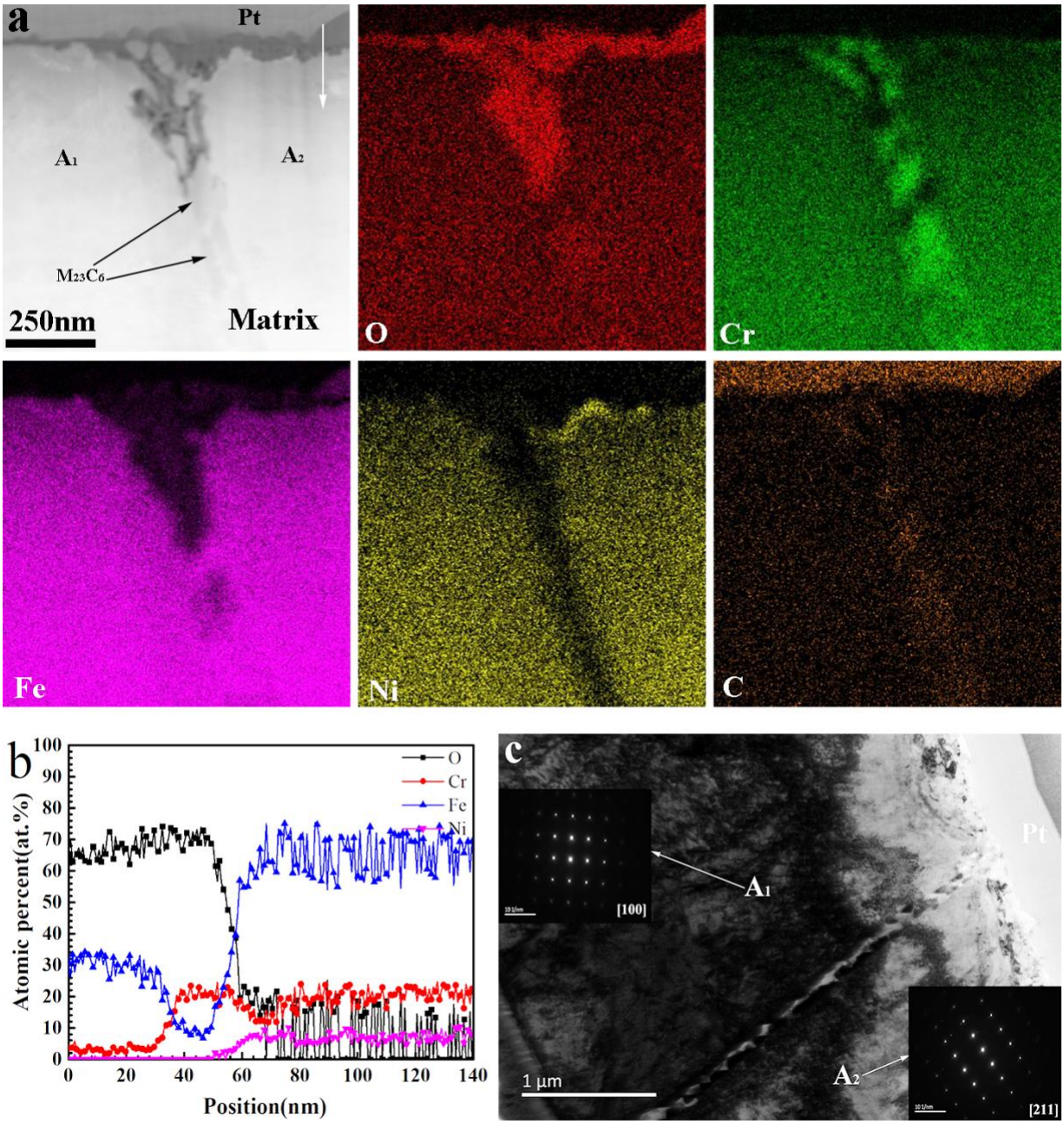

Fig. 18. (a) STEM-HAADF image of the grain boundary and the corresponding EDS maps of oxide film formed on 308L SS, (b) EDS line scan profile of the oxide film shown in (a), (c) TEM bright field image of the grain boundary and oxide film.

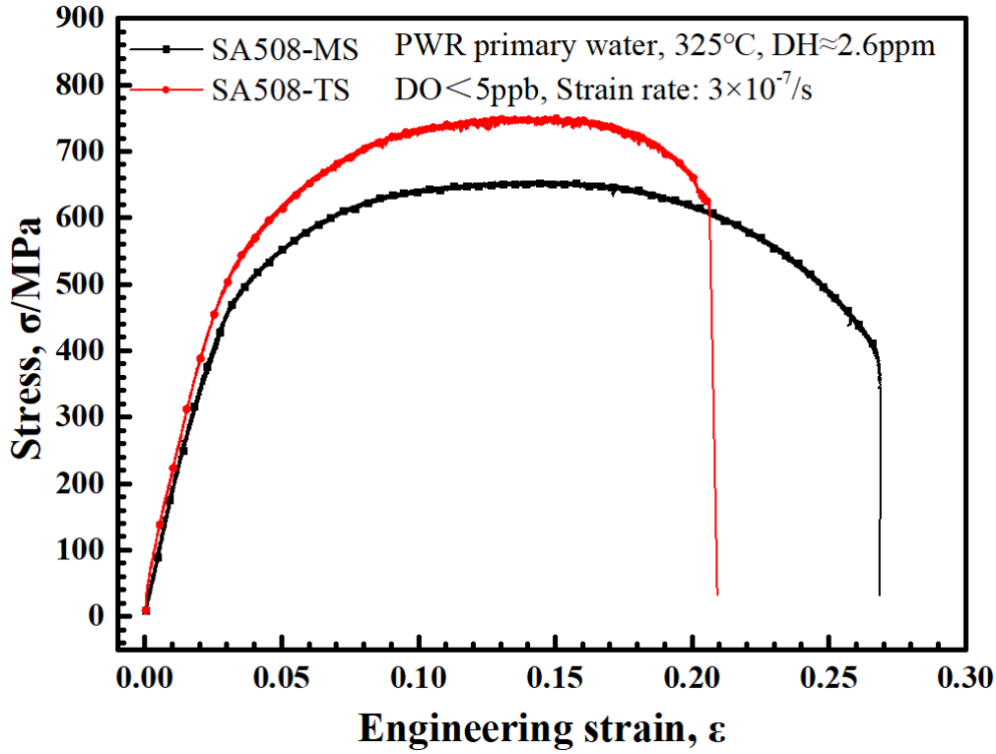

Fig. 19. Stress-strain curves at strain rate of 3×10^{-7}/s for A508III matrix and transition layer specimens in simulated PWR primary water at 325 ºC.

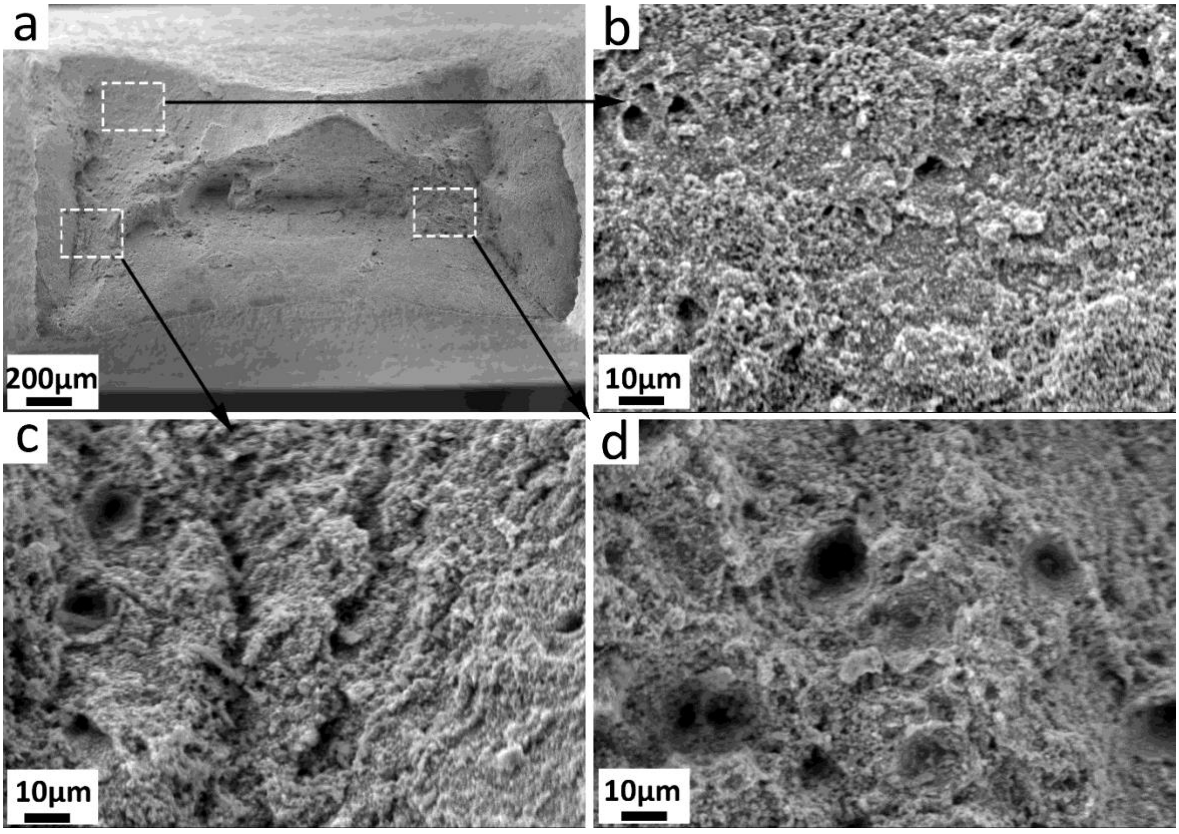

Fig. 20. SEM morphologies of the fracture surface after SSRT at 3×10^{-7}/s for A508-MS specimen in simulated PWR primary water at 325 ºC.

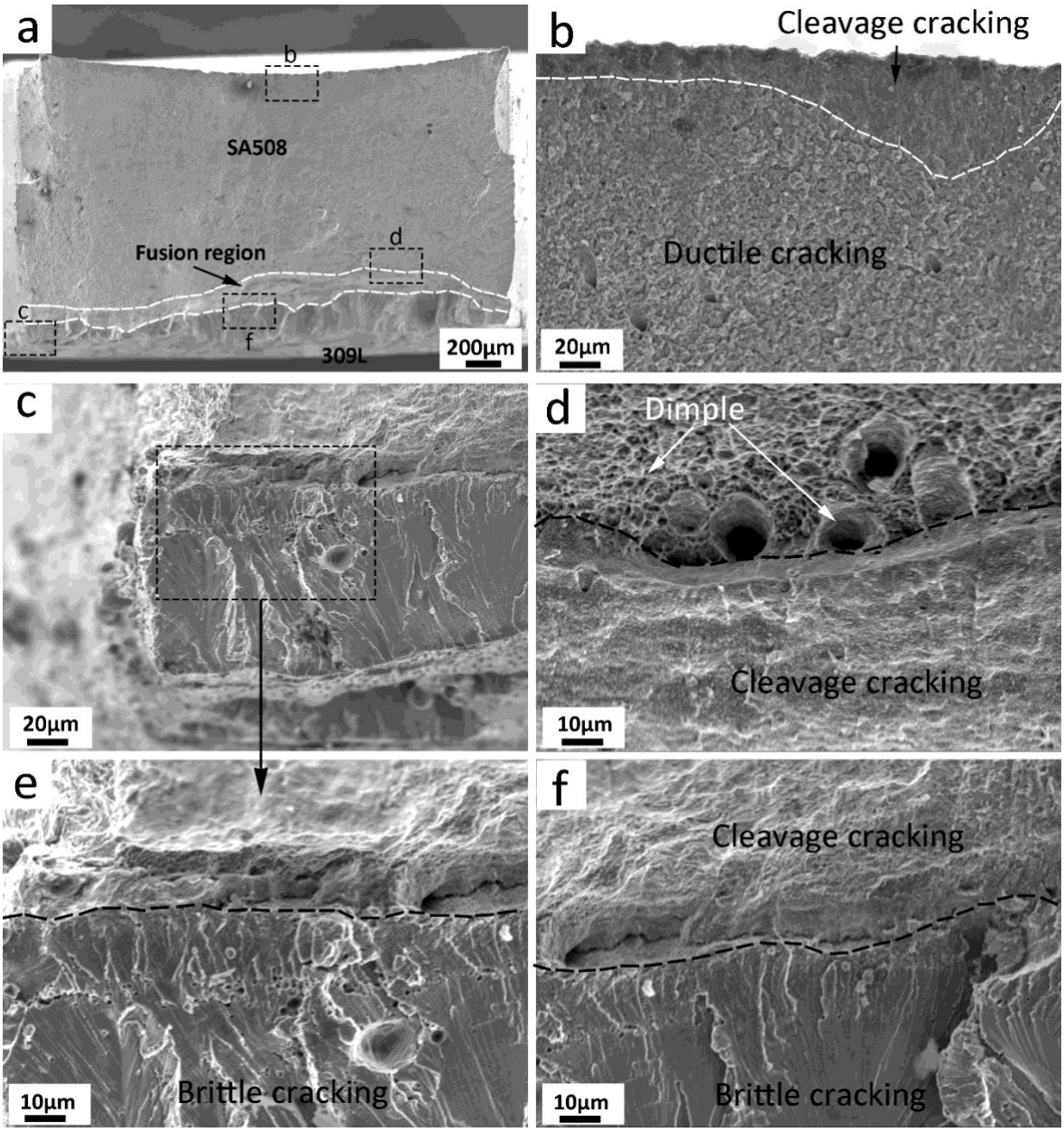

Fig. 21. SEM morphologies of the fracture surface after SSRT at 3×10^{-7}/s for A508-TS specimen in simulated PWR primary water at 325 °C.

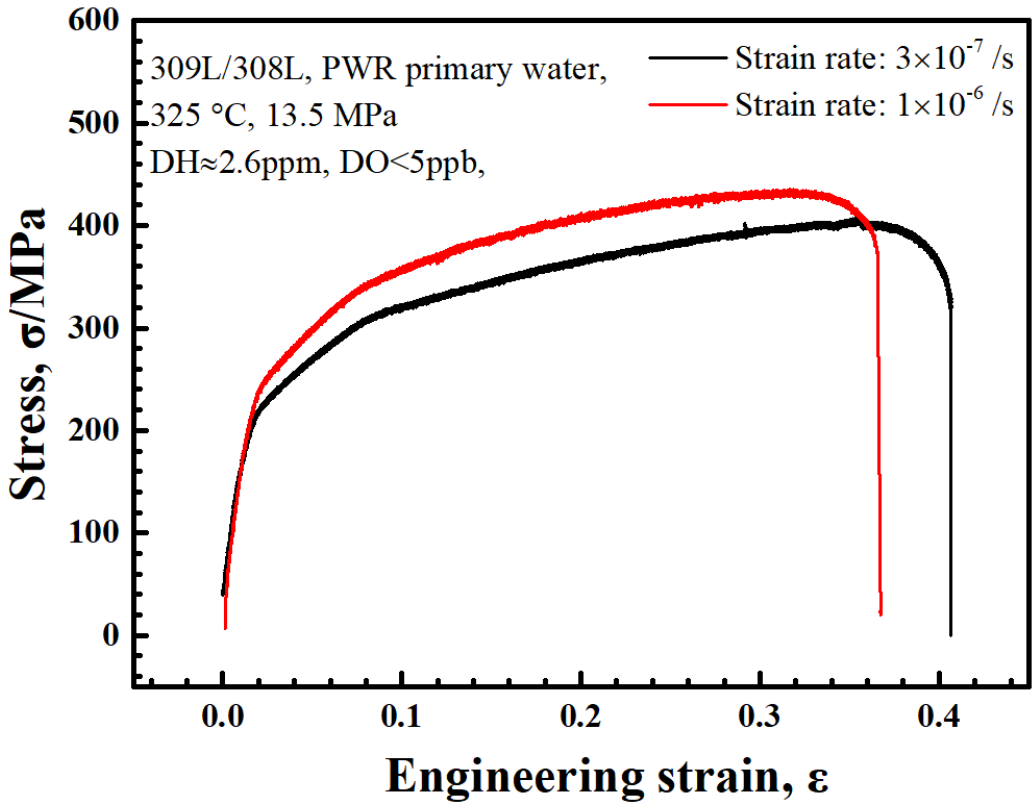

Fig. 22. Stress-strain curves at strain rate of 3×10^{-7}/s and 1×10^{-6}/s for 309L/308L SS specimen in simulated PWR primary water at 325 °C.

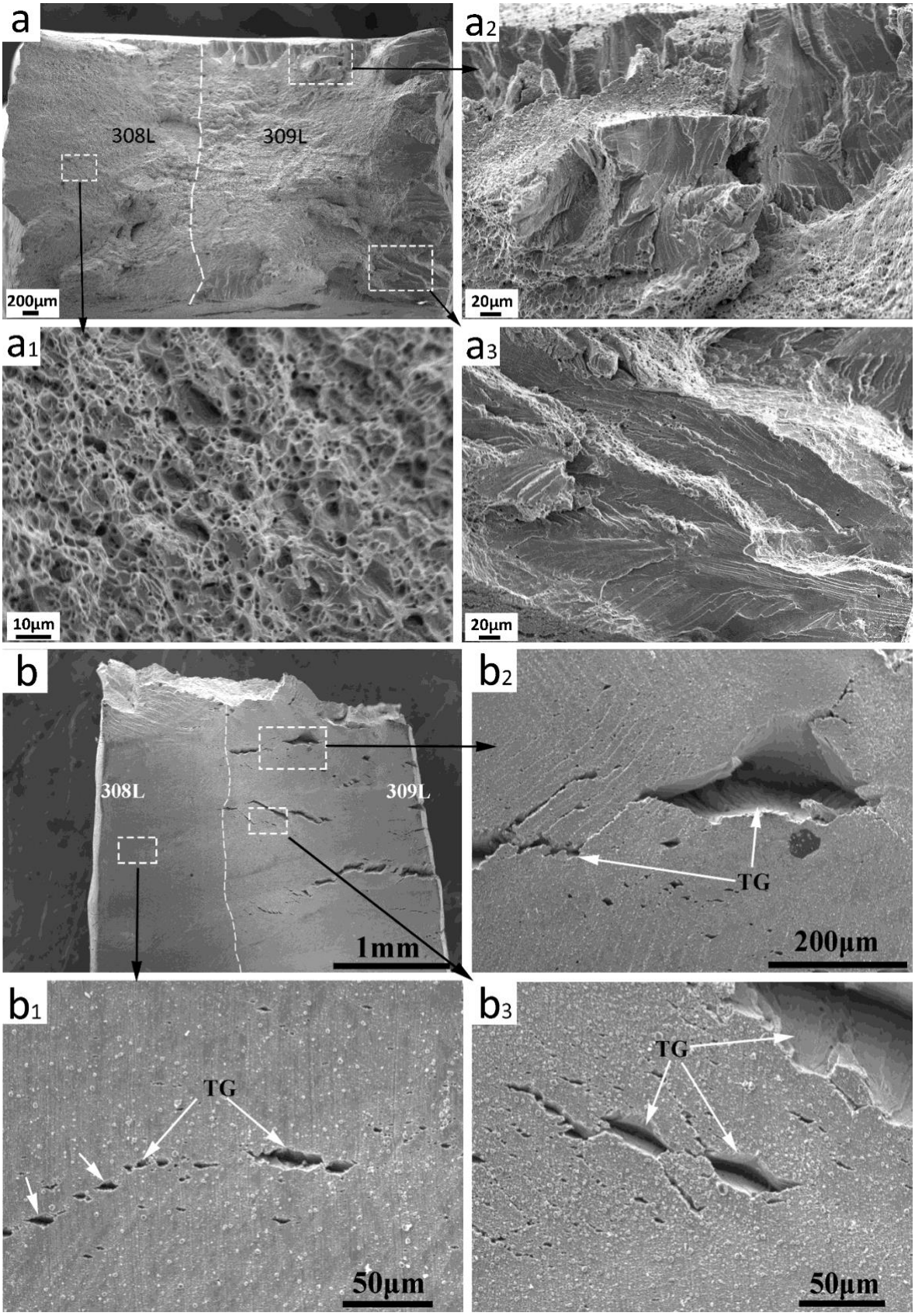

Fig. 23. SEM morphologies of the fracture surface and gauge side after SSRT at 3×10^{-7}/s for 309L/308L specimen in hydrogenated PWR primary water at 325 ºC.

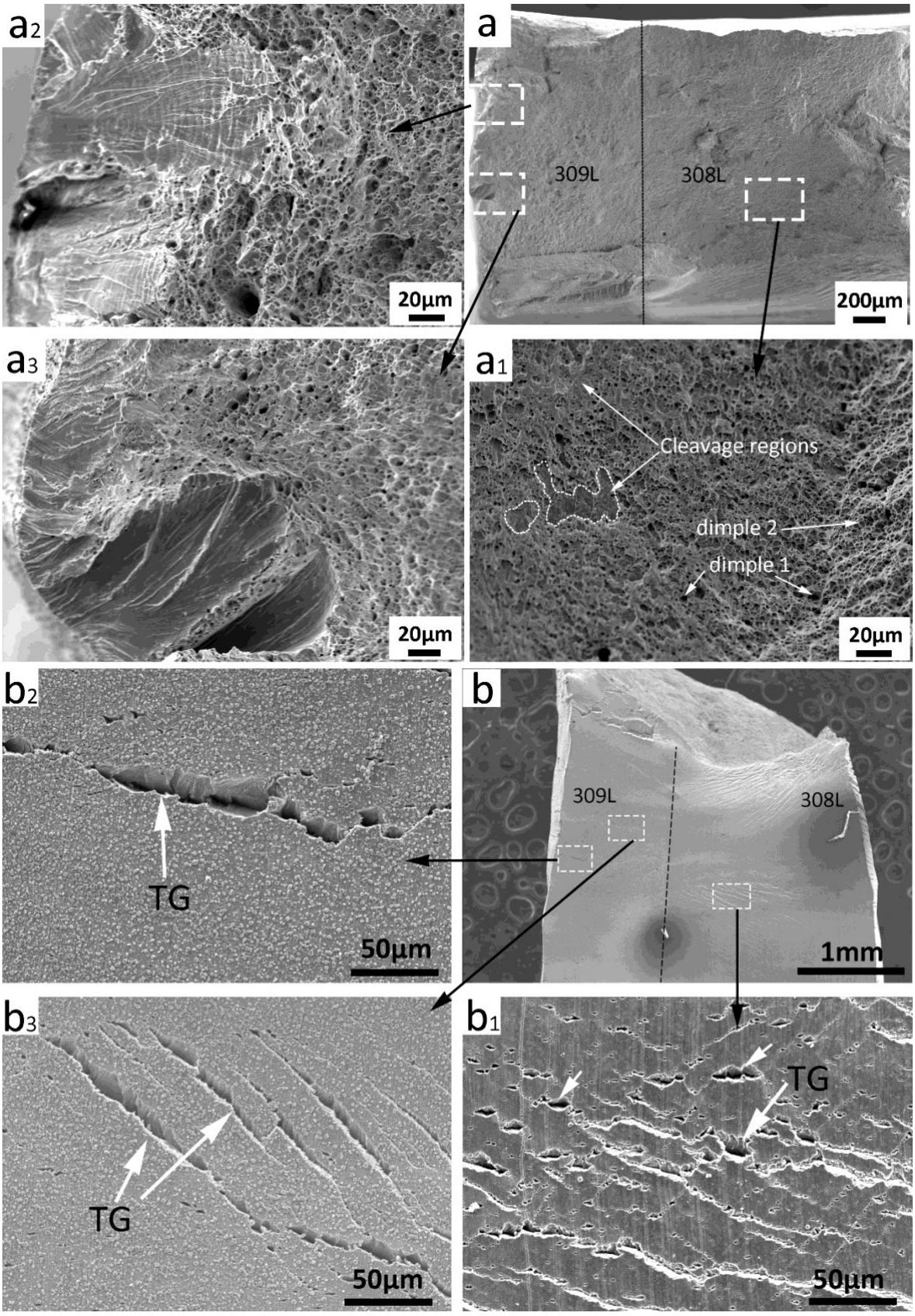

Fig. 24. SEM morphologies of the fracture surface and gauge side after SSRT at 1×10^{-6}/s for 309L/308L specimen in hydrogenated PWR primary water at 325 ºC.

Table 1. Chemical compositions of the LAS matrix and the SS cladding layers (wt. %).

Alloy	Cr	Ni	Mn	S	Cu	C	Si	Mo	Nb	Fe
A508III	0.11	0.50	1.37	0.003	0.02	0.21	0.21	0.47	<0.001	Bal.
309L	17.95	9.95	1.32	0.003	0.054	0.03	0.56	0.12	<0.001	Bal.
308L	20.05	10.27	1.77	0.002	0.045	0.03	0.86	0.096	0.001	Bal.

Table 2. Summary of the mechanical properties of the A508III-309L/308L SS claddings after SSRT tests at different strain rates.

Specimens, No.	Strain rate	YS (MPa)	UTS (MPa)	Elongation to failure (%)
A508-MS	3×10^{-7}/s	450	680	26.9
A508-TS	3×10^{-7}/s	500	740	21.0
309L/308L	3×10^{-7}/s	235	402	40.8
309L/308L	1×10^{-6}/s	245	432	36.3